Composited analyses of the chemical and physical characteristics of co-polluted days by ozone and PM$_{2.5}$ over 2013-2020 in the Beijing–Tianjin–Hebei region

Huibin Dai[1], Hong Liao[1*], Ke Li[1], Xu Yue[1], Yang Yang[1], Jia Zhu [1], Jianbing Jin[1], Baojie Li[1], Xingwen Jiang[2]

[1]Jiangsu Key Laboratory of Atmospheric Environment Monitoring and Pollution Control, Jiangsu Collaborative Innovation Center of Atmospheric Environment and Equipment Technology, School of Environmental Science and Engineering, Nanjing University of Information Science & Technology, Nanjing 210044, China

[2]Institute of Plateau Meteorology, China Meteorological Administration, Chengdu, Sichuan 610072, China

*Correspondence to: Hong Liao (hongliao@nuist.edu.cn)

Abstract.

The co-polluted days by ozone (O_3) and $PM_{2.5}$ (particulate matter with an aerodynamic equivalent diameter of 2.5 μm or less) ($O_3\&PM_{2.5}PD$) were frequently observed in the Beijing–Tianjin–Hebei (BTH) region in warm seasons (April-October) of 2013-2020. We applied the 3-D global chemical transport model (GEOS-Chem) to investigate the chemical and physical characteristics of $O_3\&PM_{2.5}PD$ by composited analyses of such days that were captured by both the observations and the model. Model results showed that, when $O_3\&PM_{2.5}PD$ occurred, the concentrations of hydroxyl radical and total oxidant, sulfur oxidation ratio, and nitrogen oxidation ratio were all high, and the concentrations of sulfate at the surface were the highest among all pollution types. We also found unique features in vertical distributions of aerosols during $O_3\&PM_{2.5}PD$; concentrations of $PM_{2.5}$ decreased with altitude near the surface but remained stable at 975-819 hPa. Process analyses showed that secondary aerosols (nitrate, ammonium and sulfate) had strong chemical productions at 913-819 hPa, which were then transported downward, resulting in the quite uniform vertical profiles at 975-819 hPa in $O_3\&PM_{2.5}PD$. The weather patterns for $O_3\&PM_{2.5}PD$ were characterized by anomalous high-pressure system at 500 hPa as well as strong southerlies and high RH at 850 hPa. The latter resulted in the strong chemical productions around 850 hPa in $O_3\&PM_{2.5}PD$. The physical and chemical characteristics of $O_3\&PM_{2.5}PD$ are quite different from those of polluted days by either O_3 alone or $PM_{2.5}$ alone, which have important implications for air quality management.

Keywords: Co-occurrence, Ozone and $PM_{2.5}$, Pollution, Meteorological parameters.

1. Introduction

42   Surface ozone (O_3) and $PM_{2.5}$ (particulate matter with an aerodynamic equivalent

43   diameter of 2.5 micrometers or less) are important air pollutants in the atmosphere that

44   have harmful effects on public health (Gao and Ji, 2018; Jiang et al., 2019), ecosystems

45   (Ren et al., 2011; Yue et al., 2017), and crops (Wang et al., 2005; Wang et al., 2007).

46   Surface O_3 is a secondary pollutant produced by photochemical oxidation of volatile

47   organic compounds (VOCs) and nitrogen oxides ($NO_x \equiv NO+NO_2$) in the presence of

48   intense ultraviolet light, and the major $PM_{2.5}$ components (nitrate (NO_3^-), ammonium

49   (NH_4^+), sulfate (SO_4^{2-}), black carbon (BC), organic carbon (OC)) are mainly caused by

50   anthropogenic emissions of aerosols and aerosol precursors. Although surface O_3 and

51    $PM_{2.5}$ have different formation mechanisms, they are coupled through the common

52   precursors (NO_x and VOCs) and photochemical reactions (Chu et al., 2020). Since 2013,

53   stringent clean air actions have been implemented to improve air quality in China (State

54   Council of the People's Republic of China, 2013, 2018). However, O_3 concentrations

55   increased unexpectedly, while $PM_{2.5}$ concentrations decreased drastically in the past

56   years (Li et al., 2019). The co-polluted days by O_3 and $PM_{2.5}$ (concentrations of both

57   O_3 and $PM_{2.5}$ exceed the national air quality standards on the same day, hereafter

58   referred to as O_3&$PM_{2.5}$PD) were also reported (Dai et al., 2019). Therefore, it is

59   fundamental to examine the chemical and physical characteristics of O_3&$PM_{2.5}$PD.

60   The Beijing–Tianjin–Hebei (BTH) region is the most populated region in northern

61   China. In the past few years, concentrations of O_3 and $PM_{2.5}$ in the BTH were among

62   the highest in China. The observations from China National Environmental Monitoring

63   Center (CNEMC) showed that the mean and maximum MDA8 (daily maximum 8-h

64   average) O_3 in North China in summer of 2019 were 83 ppb and 129 ppb, respectively,

65   and the summer mean MDA8 O_3 increased with a trend of 3.3 ppb a^{-1} over 2013–2019

66   (Li et al., 2020). Gong et al. (2020) reported that O_3 polluted days (i.e., MDA8 O_3

concentration exceeds 80 ppb) in May-July in the BTH increased from 35 days in the year of 2014 to 56 days in 2018. As for observed $PM_{2.5}$, the concentration averaged over BTH had a decreasing trend of 10 μg m^{-3} yr^{-1} over 2013-2019, and the mean value was 79 ± 17 μg m^{-3} over these years (Li et al., 2020). BTH also had the highest frequency and intensity of severe haze pollution days (i.e., days with daily mean $PM_{2.5}$ concentration exceeding 150 μg m^{-3}) in China from 2013 to 2017, with an observed mean frequency of 21.2 d yr^{-1} and an observed mean intensity of 231.6 μg m^{-3} (Dang and Liao, 2019).

The interactions between O_3 and $PM_{2.5}$ have been reported in previous studies. Zhu et al. (2019) examined the spatial-temporal characteristics of the correlations between observed O_3 and $PM_{2.5}$ at 1497 sites in China for 2016 and found that O_3–$PM_{2.5}$ had the highest positive correlations (correlation coefficients > +0.7) in July in southern China and the largest negative correlations (r values < −0.5) during January in northern China. Li et al. (2019) used the GEOS-Chem model to analyze the O_3-$PM_{2.5}$ relationship in northern China and found that O_3 production was suppressed under high $PM_{2.5}$ conditions ($PM_{2.5}$ concentrations > 60 μg m^{-3}) because of the reactive uptake of hydrogen oxide radicals (HO_x) by aerosol particles. Chu et al. (2020) analyzed the observed daily $PM_{2.5}$ and O_3 concentrations in 114 cities in China during years of 2013-2018 and found that the correlations between O_3 and $PM_{2.5}$ tended to change from negative in 2013 to positive in 2018 in China as air quality improved.

Few previous studies have examined the co-occurrence of O_3 and $PM_{2.5}$ pollution (MDA8 O_3 > 80 ppb and $PM_{2.5}$ > 75 μg m^{-3}). Zong et al. (2021) used the obliquely rotated principal component analysis in the T-mode (T-PCA) method to identify the synoptic weather pattern associated with O_3&$PM_{2.5}$PD in eastern China during summer of 2015–2018, and found that O_3&$PM_{2.5}$PD were associated with a stable

western Pacific subtropical high ridge, which brought warm and moist air flow from the East China Sea to the eastern China to promote hygroscopic growth of fine particulate matter in BTH and northern YRD. Dai et al. (2021) analyzed $O_3\&PM_{2.5}PD$ in the YRD for April-October of 2013-2019 by using observations and reported that the co-polluted days occurred mainly in April (29.6% of co-polluted days occurred in April), May (23.0%), June (19.5%), and October (10.8%) under meteorological conditions of higher relative humidity, higher surface air temperature, and lower wind speed relative to the days with O_3 pollution alone. Qin et al. (2021) investigated $O_3\&PM_{2.5}PD$ by using the hourly observed concentrations of water-soluble ions, OC, and elemental carbon (EC) in 2019 in cities of Nanjing and Changzhou. They found that inorganic aerosols mainly existed as NH_4NO_3 and the correlation coefficients between the secondary components NO_3^-, NH_4^+, and SO_4^{2-} were relatively high during $O_3\&PM_{2.5}PD$ in 2019, indicating a significant formation of secondary inorganic aerosols. Although these studies have discussed the meteorological conditions and some chemical characteristics of $O_3\&PM_{2.5}PD$, the understanding of $O_3\&PM_{2.5}PD$ was quite limited because of the limited observations of chemical species involved.

In this work, we take advantage of the comprehensive chemical mechanism of the global chemical transport model to have better understanding of $O_3\&PM_{2.5}PD$. We apply the 3-D global chemical transport model (GEOS-Chem) to simulate $O_3\&PM_{2.5}PD$ in BTH in years of 2013-2020, and investigate the chemical and physical characteristics of $O_3\&PM_{2.5}PD$ by composited analyses of such days that are captured by both the observations and the model. The objectives of this study are: 1) to examine the underlying chemical mechanisms for $O_3\&PM_{2.5}PD$ in BTH for warm seasons (April-October) of 2013-2020 by comparing $O_3\&PM_{2.5}PD$ with polluted days by O_3 alone or by $PM_{2.5}$ alone, and 2) to identify the weather patterns that are

associated with O_3&$PM_{2.5}$PD in BTH. The observations, the reanalyzed

meteorological data, the GEOS-Chem model, and the process analysis are described

in Section 2. The observed O_3&$PM_{2.5}$PD are presented in Section 3.1. The evaluation

of simulated concentrations of O_3 and $PM_{2.5}$ as well as the simulated pollution days by

O_3 and/or $PM_{2.5}$ are shown in Section 3.2. The underlying mechanisms of

O_3&$PM_{2.5}$PD are shown in Section 3.3. In Section 3.4, the meteorological conditions

for the co-occurrence of O_3 and $PM_{2.5}$ pollution are investigated. The conclusions are

presented in Section 4.

2. Methods

2.1 Observed O_3 and $PM_{2.5}$ concentrations

Hourly concentrations of $PM_{2.5}$ and O_3 in China over the years of 2013-2020

were taken from the public website of CNEMC (https://air.cnemc.cn:18007/, last

access: 17 November 2022). To ensure data quality, the daily mean $PM_{2.5}$

concentration was calculated when there were valid data for more than 20 h during

that day and the MDA8 O_3 concentration was calculated when there were valid data

for at least 6 h for each 8 h. For the calculation of monthly and annual mean

concentrations, the number of days with valid concentrations had to be more than 15

in each month. The spatial distribution of the 79 valid sites within BTH (37-41°N,

114-118°E, the black rectangle) is shown in Fig. 1. For model evaluation, the

observed concentrations were averaged over sites within each of the 0.5° latitude ×

0.625° longitude MERRA-2 grid cell. There are 18 model grids in BTH. Note that the

observed O_3 concentrations from this network have a unit of $\mu g\ m^{-3}$. For the

consistency of observed and simulated O_3 concentrations, 1 $\mu g\ m^{-3}$ of O_3 is

approximately 0.5 ppb under the conditions of 298 K and 1013 hPa. The observed O_3

142   concentrations reported by the CNEMC were under standard conditions of 273 K and

143   1013 hPa before 31 August 2018 and were under standard conditions of 298 K and

144   1013 hPa afterwards (http://www.mee.gov.cn/

145   xxgk2018/xxgk/xxgk01/201808/t20180815_629602.html, last access: 17 November

146   2022), which were accounted for as O_3 concentrations were converted to ppb.

147     According to the National Ambient Air Quality Standard of China (GB3095-

148   2012), O_3 ($PM_{2.5}$) concentration exceeds the national air quality standard if the MDA8

149   O_3 (daily mean $PM_{2.5}$) concentration is higher than 160 μg m^{-3} (75 μg m^{-3}). In this

150   study, we define O_3 polluted days (hereafter called 'O$_3$PD') for days with MDA8 O_3

151   concentration > 160 μg m^{-3}, $PM_{2.5}$ polluted days (hereafter called 'PM$_{2.5}$PD') with

152   daily mean $PM_{2.5}$ concentration > 75 μg m^{-3}, and the co-pollution days by O_3 and

153   $PM_{2.5}$ (O$_3$&PM$_{2.5}$PD) with daily MDA8 O_3 concentration > 160 μg m^{-3} as well as the

154   daily mean $PM_{2.5}$ concentration > 75 μg m^{-3}.

155

156   **2.2 Reanalyzed meteorological fields**

157     Meteorological fields were obtained from the Version 2 of Modern Era

158   Retrospective-analysis for Research and Application (MERRA2), which were

159   generated by the NASA Global Modeling and Assimilation Office (GMAO). The

160   MERRA2 data have a horizontal resolution of 0.5° latitude × 0.625° longitude and

161   72 vertical layers (Molod et al., 2015). To analyze the meteorological conditions for

162   O$_3$&PM$_{2.5}$PD, vertical pressure velocity (OMEGA), planetary boundary layer height

163   (PBLH), temperature (T), relative humidity (RH), surface incoming shortwave flux

164   (SWGDN) are used. Note that the temporal resolution for PBLH, T, and SWGDN is

165   1h, and that for OMEGA and RH is 3h. Daily mean geopotential heights at 850 and

166   500 hPa from the National Center for Environmental Prediction (NCEP) and National

167   Center for Atmospheric Research (NCAR) global reanalysis with a resolution of 2.5°

168   latitude by 2.5° longitude are also utilized in this study.

169

170   **2.3 Observed aerosol optical depth**

171   We obtained the version 3 datasets of observed daily aerosol optical depth

172   (AOD) of level 2 (improved cloud screened and quality-assured) from Aerosol

173   Robotic Network (AERONET, https://aeronet.gsfc.nasa.gov/new_web/index.html, last

174   access: 17 November 2022) established by NASA and LOA-PHOTONS (Giles et al.,

175   2019). Three sites in the BTH region have observations available over 2013-2020,

176   including Beijing (39.97°N, 116.38°E), Beijing-CAMS (39.93°N, 116.31°E), and

177   Xianghe (39.75°N, 116.96°E). The AOD values at 440 nm and 675 nm at these three

178   sites are analyzed in this study.

179

180   **2.4 GEOS-Chem model**

181   We simulated O_3 and $PM_{2.5}$ using the nested version of the 3-D global chemical

182   transport model (GEOS-Chem, version 11-01) driven by the MERRA2

183   meteorological data. The nested domain was set over Asia (60°-150°E,11°S-55°N)

184   with a horizontal resolution of 0.5° latitude × 0.625° longitude, and the chemical

185   boundary conditions were provided by the global GEOS-Chem simulation with 2.5°

186   latitude × 2.5° longitude horizontal resolution.

187   The GEOS-Chem model includes fully coupled O_3-NO_x-hydrocarbon and

188   aerosol chemistry mechanism (Bey et al., 2001; Pye et al., 2009) to simulate aerosols

189   including SO_4^{2-} (Park et al., 2004), NO_3^- (Pye et al., 2009), NH_4^+, BC and OC (Park

190   et al., 2003), mineral dust (Fairlie et al., 2007), and sea salt (Alexander et al., 2005) as

191   well as the gas-phase pollutants such as NO_x and O_3. Over the Asian domain, the

192   anthropogenic emissions of OC, BC, carbon monoxide (CO), sulfur dioxide (SO_2),

193   NO_x, ammonia (NH_3), and VOCs were obtained from the Multi-resolution Emission

194   Inventory for China (MEIC), which includes emissions from industry, power,

195   residential and transportation sectors for years of 2014-2017 (Li et al., 2017; Zheng et

196   al., 2018), 2019 and 2020 (Zheng et al., 2021). Emissions in 2018 were obtained by

197   the interpolation of those in 2017 and 2019 for each grid due to the lack of publicly

198   accessible emission inventories for that year. The biogenic emissions in GEOS-Chem

199   are simulated using MEGAN v2.1 (Guenther et al., 2012).

200   The hourly O_3 and $PM_{2.5}$ concentrations for the years of 2013-2020 were

201   simulated by the GEOS-Chem model which were driven by MERRA-2

202   meteorological fields. The model was spined up for 6 months before the integration

203   over the studied time period.

204

205   **2.5 Process analysis**

206   Process analysis (PA) was applied to identify the relative importance of

207   atmospheric processes in O_3&$PM_{2.5}$PD. PA has been widely used in previous studies

208   to examine the key processes contributing to air pollution episodes (Gonçalves et al.,

209   2009; Dang and Liao, 2019; Gong and Liao, 2019) as well as the interannual and

210   decadal variations of air pollutants (Mu and Liao, 2014; Lou et al., 2015). Five major

211   processes that influence O_3 and $PM_{2.5}$ concentrations were diagnosed at every time

212   step, including net chemical production, dry deposition, horizontal advection, vertical

213   advection, and diffusion, for the regional pollution days (days with more than half of

214   the sites in BTH experiencing pollutions). We carried out PA for O_3SPD (exclude

215   O_3&$PM_{2.5}$PD from O_3PD), $PM_{2.5}$SPD (exclude O_3&$PM_{2.5}$PD from $PM_{2.5}$PD), and

216   O_3&$PM_{2.5}$PD over BTH.

217

218   **3. Results**

219   **3.1 Observed polluted days by O_3 and $PM_{2.5}$**

220   Figure 1a shows the spatial distributions of observed numbers of O_3PD,

221     $PM_{2.5}$PD, and O_3&$PM_{2.5}$PD summed over the warm seasons (April-October) of 2013-

222   2020. The spatial distributions of polluted days in each year are shown in Fig. S1. The

223   numbers of O_3PD, $PM_{2.5}$PD, and O_3&$PM_{2.5}$PD were high in BTH, which were,

224   respectively, 524.3 344.6, and 128.1 days from observations, as the values were

225   averaged over all sites in BTH. The high numbers of O_3PD, $PM_{2.5}$PD, and

226   O_3&$PM_{2.5}$PD in BTH were associated with the highest anthropogenic emissions (NO_x

227   and NMVOCs) in this region (Dang et al., 2021).

228   Figure 1b shows the numbers of days averaged over all sites in BTH for non-

229   polluted days (NPD, MDA8 O_3 < 80 ppb and $PM_{2.5}$ < 75 μg m^{-3}), O_3PD,

230   O_3&$PM_{2.5}$PD, and $PM_{2.5}$PD in each month of warm seasons from 2013 to 2020. O_3PD

231   and O_3&$PM_{2.5}$PD mainly occurred in May, June, and July, while $PM_{2.5}$PD mainly

232   appeared in April and October. The monthly numbers of O_3&$PM_{2.5}$PD ($PM_{2.5}$PD)

233   declined from 2013 to 2020, with the fastest drop in June, from 7.5 (17.1) days in

234   June 2013 to 1.8 (1.8) days in June 2020. On the contrary, the numbers of O_3PD kept

235   increasing, especially in June, from 10.9 days in June 2013 to 23.6 days in June 2020.

236   The reductions in O_3&$PM_{2.5}$PD were associated with the large reductions in $PM_{2.5}$

237   since the implementation of the Clean Air Action in 2013.
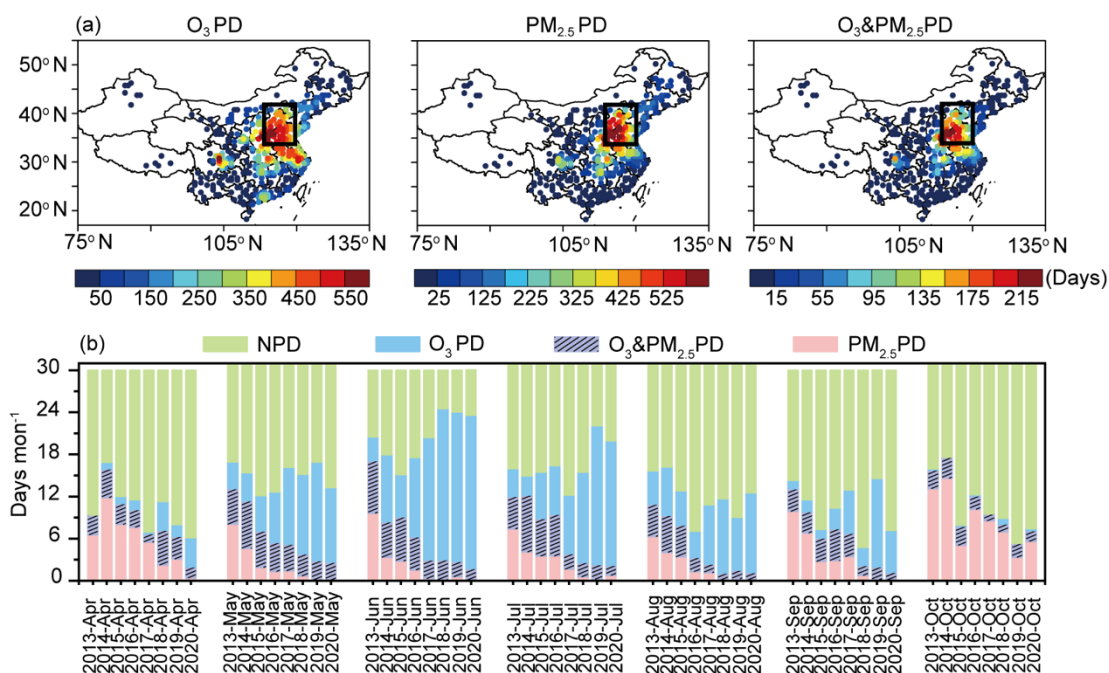
Figure 1. (a) Spatial distributions of observed numbers of O_3PD, $PM_{2.5}PD$, and

$O_3\&PM_{2.5}PD$ summed over April-October of 2013-2020. The solid black rectangle

indicates the BTH region. (b) The observed numbers of NPD (non-polluted days,

green), O_3PD (blue + purple with slashes), $O_3\&PM_{2.5}PD$ (purple with slashes), and

$PM_{2.5}PD$ (pink + purple with slashes) averaged over all sites in BTH from April to

October in 2013 to 2020.

Figure 2a shows the linear trends of observed O_3PD, $PM_{2.5}PD$, and $O_3\&PM_{2.5}PD$

in warm seasons of 2013-2020 averaged over the BTH. O_3PD showed an upward

trend of 7.9 days yr^{-1} from 2013 to 2020. However, the numbers of $PM_{2.5}PD$ and

$O_3\&PM_{2.5}PD$ decreased over 2013-2020, with linear trends of -11.2 and -3.4 days yr^{-1},

respectively. Figure 2b shows the changes in percentage of $O_3\&PM_{2.5}PD$ in $PM_{2.5}PD$

from 2013 to 2020 for each month. It should be noted that, when $PM_{2.5}PD$ occurred,

the proportions of $O_3\&PM_{2.5}PD$ had an upward trend from 2013 to 2020. In May,

June, August, and September of 2020, the proportions of $O_3\&PM_{2.5}PD$ in $PM_{2.5}PD$

reached 100%, indicating that $PM_{2.5}$ pollution was accompanied by O_3 pollution in

254 recent years.

255
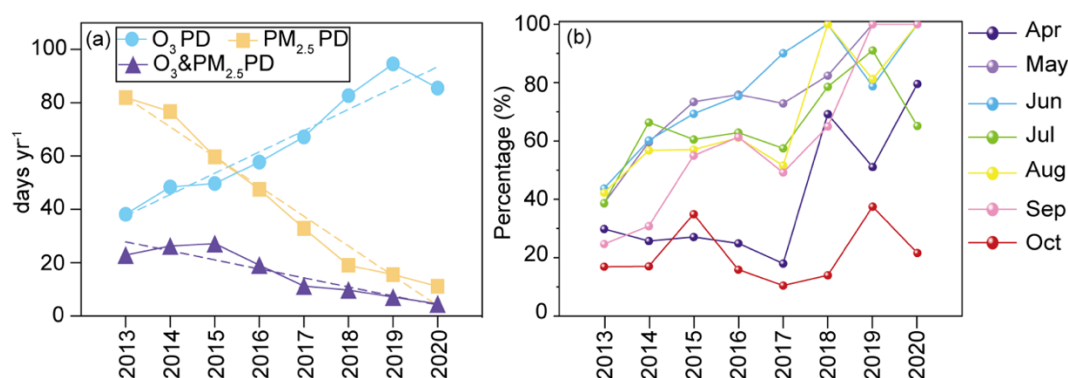
Figure 2. (a) The trends of observed O_3PD, $PM_{2.5}PD$, and $O_3\&PM_{2.5}PD$ in warm

seasons from 2013 to 2020 averaged over all sites in BTH. The blue, yellow and purple

solid lines (dashed lines) represent the numbers (liner trend) of O_3PD, $PM_{2.5}PD$, and

$O_3\&PM_{2.5}PD$, respectively. (b) The percentage of $O_3\&PM_{2.5}PD$ in $PM_{2.5}PD$ for April

to October in 2013 to 2020. The polluted days were averaged over all sites in BTH.

261

3.2 Simulated polluted days and model evaluation

3.2.1 Simulated surface-layer MDA8 O_3 and $PM_{2.5}$ concentrations

Figures 3a and 3b show, respectively, the spatial distributions of simulated and

observed surface-layer concentrations of MDA8 O_3 and $PM_{2.5}$ in China, as the

concentrations are averaged over the warm seasons (April-October) of 2013-2020.

The concentrations of MDA8 O_3 and $PM_{2.5}$ were both high in BTH. Averaged over

BTH and the studied time period, the observed concentrations of MDA8 O_3 and $PM_{2.5}$

were 58.1 ppb and 60.3 $\mu g\ m^{-3}$, respectively, while the simulated values were 68.0 ppb

and 61.1 $\mu g\ m^{-3}$, respectively. Figures 3c and 3d compare the time series of observed

and simulated daily MDA8 O_3 and $PM_{2.5}$ concentrations averaged over the BTH. The

simulated daily concentrations of MDA8 O_3 ($PM_{2.5}$) in eight warm seasons have a

normalized mean bias (NMB) of 7.9% (10.6%). The model generally captures the

daily variations (peaks and troughs) in the observed MDA8 O_3 and $PM_{2.5}$

concentrations, with R values of 0.80 and 0.72, respectively. It should be noted that

mineral dust and sea-salt aerosols were not considered in this study, because they are

not the major aerosol components in China and the concentrations are generally low

based on previous measurements (Xuan et al., 2000; Ye et al., 2003; Duan et al., 2006;

Zhao et al., 2013). However, excluding dust and sea salt may lead to low biases in

simulated $PM_{2.5}$ concentrations.

Due to the lack of the publicly accessible long-term observations of $PM_{2.5}$

components in China, we compared the simulated SO_2 and NO_2 (precursors for SO_4^{2-}

and NO_3^-) with observations from CNEMC in Fig. S2. The simulated daily mean

concentrations of NO_2 (SO_2) agree well with the observations from CNEMC with R

of 0.82 (0.78) and MB of -14.9% (9.3%).
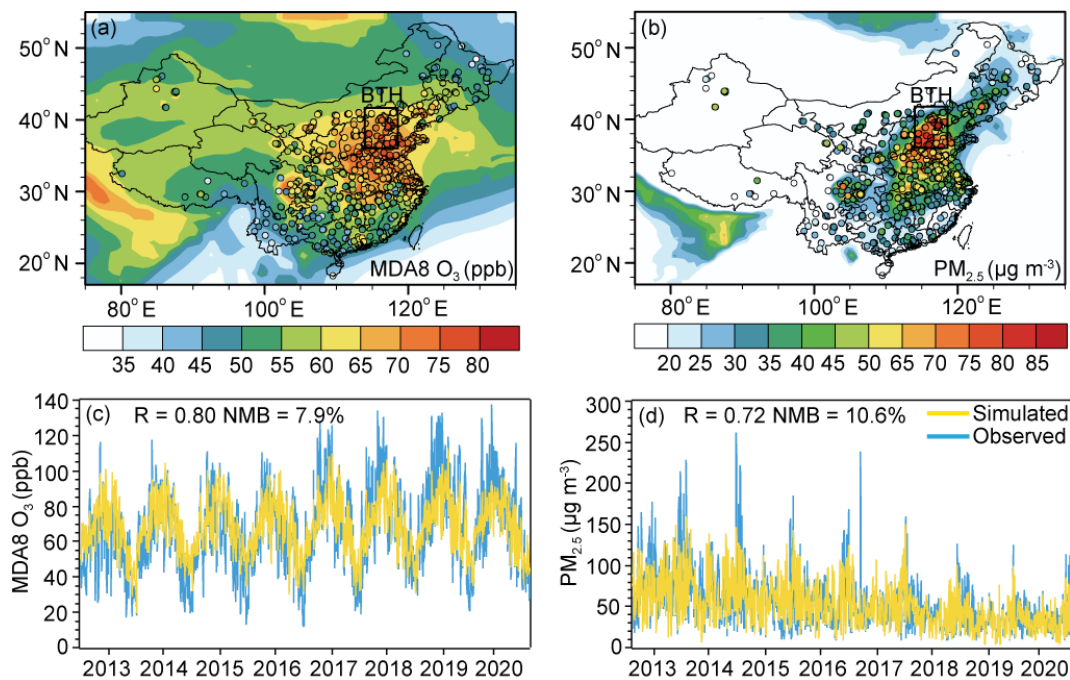
Figure 3. Spatial distributions of simulated (shades) and observed (CNEMC, dots)

surface-layer concentrations of (a) MDA8 O_3 (ppb) and (b) $PM_{2.5}$ ($\mu g\ m^{-3}$) averaged

over the eight warm seasons (April to October, 2013–2020). The solid black rectangle

in (a) and (b) indicates the BTH region. Simulated and observed daily concentrations

291   of surface-layer (c) MDA8 O_3 and (d) $PM_{2.5}$ averaged over BTH. The correlation

292   coefficient (R) and normalized mean bias (NMB) are also shown for (c) and (d).

293    $NMB = (\sum_{i=1}^{N}(M_i - O_i)/\sum_{i=1}^{N}(O_i)) \times 100\%$, where O_i and M_i are the observed and

294   simulated concentrations, respectively, i refers to the ith day, and N is the total number

295   of days.

296   **3.2.2 Simulated O_3PD, $PM_{2.5}$PD, and O_3&$PM_{2.5}$PD**

297   Figure S3 shows the capability of the model in capturing the polluted days.

298   Although the GEOS-Chem model well reproduces the spatial distributions of observed

299   MDA8 O_3 and $PM_{2.5}$ concentrations, it underestimates the numbers of O_3PD, $PM_{2.5}$PD,

300   and O_3&$PM_{2.5}$PD because of the model's deficiency in capturing the peak

301   concentrations of air pollutants. Such deficiency was also reported in previous studies

302   that used the GEOS-Chem model or the weather Research and Forecasting with

303   Chemistry (WFR-chem) model (Zhang et al., 2016; Ni et al., 2018; Gong and Liao,

304   2019; Dang and Liao, 2019). Therefore, to identify O_3PD, $PM_{2.5}$PD, and O_3&$PM_{2.5}$PD

305   using model results, we utilized lower thresholds by considering the NMBs of simulated

306   MDA8 O_3 and $PM_{2.5}$ concentrations in each of 18 grids of BTH. Taking the grid of

307   Beijing as an example, simulated MDA8 O_3 and $PM_{2.5}$ had NMBs of -22.0% and -

308   26.9%, respectively, as the simulated concentrations were compared with observations

309   for days with observed concentrations higher than the national air quality standards over

310   the warm seasons of 2013-2020. We then adjusted the threshold of O_3PD in this grid to

311   be 62.4 ppb (80 ppb×78%) and that of $PM_{2.5}$PD to be 54.8 $\mu g \ m^{-3}$ (75 $\mu g \ m^{-3}$×73.1%).

312   These adjusted thresholds were also used to identify O_3&$PM_{2.5}$PD. Such approach was

313   also used in previous studies to better capture the pollution events based on the

314   simulations (Dang and Liao, 2019; Gong and Liao, 2019). With the adjusted thresholds,

315   56-93% of the observed O_3PD, $PM_{2.5}$PD, and O_3&$PM_{2.5}$PD can be captured by the

316   model (Fig. S3e).

3.2.3 Simulated O_3SPD, $PM_{2.5}SPD$, and $O_3\&PM_{2.5}PD$

318   Since O_3PD or $PM_{2.5}PD$ encompasses $O_3\&PM_{2.5}PD$, we further define O_3 single

319   pollution days (hereafter called "O_3SPD", which is to exclude $O_3\&PM_{2.5}PD$ from O_3PD)

320   and $PM_{2.5}$ single pollution days (hereafter called "$PM_{2.5}SPD$", which is to exclude

321     $O_3\&PM_{2.5}PD$ from $PM_{2.5}PD$) for the purpose of obtaining the characteristics of

322   different polluted days. Figures 4a and 4b show, respectively, the spatial distributions

323   of numbers of O_3SPD, $PM_{2.5}SPD$, and $O_3\&PM_{2.5}PD$ from observations and from the

324   GEOS-Chem model using the adjusted thresholds. Considering the total of polluted

325   days in 18 grids in BTH, observed O_3SPD, $PM_{2.5}SPD$, and $O_3\&PM_{2.5}PD$ were,

326   respectively, 3937, 3698, and 2024 days, in which 75.0% (2954/3937), 58.1%

327   (2148/3698), and 79.7% (1614/2024) were captured by observation and simulation

328   simultaneously (Fig. 4c). In addition, the numbers of observed and captured O_3SPD,

329     $PM_{2.5}SPD$, and $O_3\&PM_{2.5}PD$ in each month are shown in Fig. S4. The model has a

330   fairly good capability of capturing the observed polluted days in each month.

331
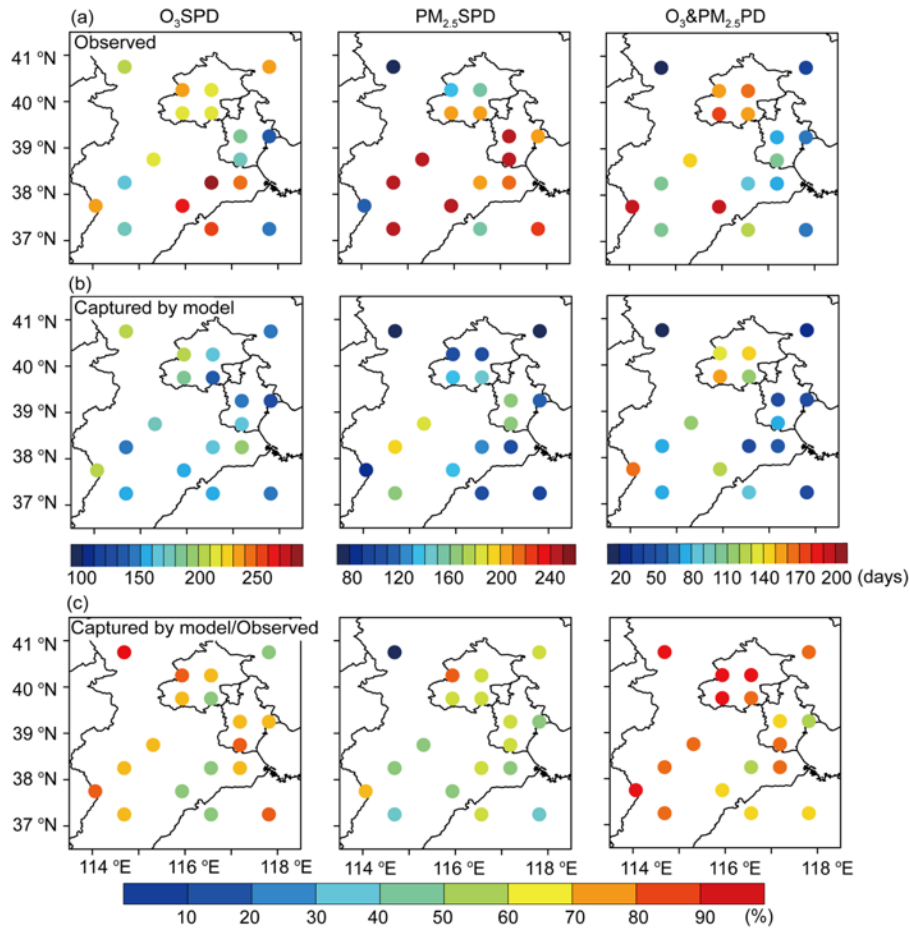
Figure 4. Spatial distributions of (a) observed numbers of O_3SPD, $PM_{2.5}$SPD, and

O_3&$PM_{2.5}$PD, (b) numbers of polluted days that were observed and also captured by

the GEOS-Chem model with adjusted thresholds, and (c) percentages of observed

polluted days that were captured by the model with adjusted thresholds. The values

were calculated for the warm months (April to October) of 2013-2020.

337

3.3 Chemical characteristics of polluted days by O_3 and $PM_{2.5}$

In this section, to investigate the chemical characteristics of O_3SPD, $PM_{2.5}$SPD

and O_3&$PM_{2.5}$PD, we present first the simulated atmospheric oxidants in 3.3.1, and

then show the simulated surface concentrations and vertical profiles of $PM_{2.5}$ and

MDA8 O_3 in 3.3.2 and 3.3.3, respectively, followed by the process analysis in 3.3.4.

The observed AOD values to verify the model results are presented in 3.3.5.

3.3.1 Atmospheric oxidants of O₃SPD, PM₂.₅SPD, and O₃&PM₂.₅PD

Figure 5 shows the boxplots of daily concentrations of hydroxyl radical (OH) and total oxidant (O_x = O_3 + NO_2) from the model for days of O₃SPD, PM₂.₅SPD, and O₃&PM₂.₅PD that were observed and also captured by the model (samples in Fig. 4b) in the warm seasons of 2013-2020 in 18 grids of BTH. The levels of OH and O_x characterize the atmospheric oxidation capacity, following Hu et al. (2020) and Chan et al. (2017). The concentrations of OH were the highest in O₃SPD, with an averaged value of 2.8×10^6 molec cm^{-3}, followed by that in O₃&PM₂.₅PD (2.0×10^6 molec cm^{-3}) and in PM₂.₅SPD (1.0×10^6 molec cm^{-3}). Due to the lack of publicly accessible observations of OH in BTH, we compare the simulated OH concentrations with observations reported in the literature (Table S1). The simulated OH concentrations agree closely with the observed values. In Wangdu of BTH, while the observed daily maximum OH concentrations in summer of 2014 were in the range of $5\text{-}15 \times 10^6$ molec cm^{-3} (Tan et al., 2016), the simulated OH concentrations in the same time period in this work were $3.7\text{-}9.5 \times 10^6$ molec cm^{-3}. In Beijing in summer of 2017, the observed daily mean OH concentration was 5.8×10^6 molec cm^{-3} (Woodward et al., 2020) and our simulated value was 2.4×10^6 molec cm^{-3}.

The mean values of O_x were, respectively, 178.7, 118.1, and 184.1 μg m^{-3} in O₃SPD, PM₂.₅SPD, and O₃&PM₂.₅PD, indicating that the atmospheric oxidation capacity was strong in O₃&PM₂.₅PD, which favored the production of secondary components of PM₂.₅. Figure 5 also shows sulfur oxidation ratio (SOR, n-SO_4^{2-} / (n-SO_4^{2-} + n-SO_2), where n-SO_4^{2-} and n-SO_2 are the concentrations of SO_4^{2-} and SO_2, respectively) and nitrogen oxidation ratio (NOR, n-NO_3^- / (n-NO_3^- + n-NO_2), where n-NO_3^- and n-NO_2 are the concentrations of NO_3^- and NO_2, respectively). SOR and NOR are measures of the conversion degrees of sulfur and nitrogen, respectively (Zhu et al.,

369 2019). In O_3SPD, $PM_{2.5}$SPD, and O_3&$PM_{2.5}$PD, the averaged values of SOR were

370 50.0%, 36.7%, and 49.7%, and those of NOR were 55.4%, 70.0%, and 70.2%,

371 respectively. The high SOR and NOR in O_3&$PM_{2.5}$PD indicated the strong formation

372 of SO_4^{2-} and NO_3^- that were promoted by high atmospheric oxidation capacity. The

373 monthly variations of OH, O_x, and SOR were similar (Fig. 5), with the highest values

374 in summer, owing to the high temperature that promoted high concentrations of

375 oxidants and SOR. It is interesting that SOR and O_x values were higher in O_3&$PM_{2.5}$PD

376 than in O_3SPD or in $PM_{2.5}$SPD during May-August. Similarly, NOR values were higher

377 in O_3&$PM_{2.5}$PD than in O_3SPD or in $PM_{2.5}$SPD in May and July-September. Overall,

378 the O_3&$PM_{2.5}$PD occurred with high levels of atmospheric oxidants, SOR, and NOR,

379 leading to combined increases in O_3 and $PM_{2.5}$ concentrations.
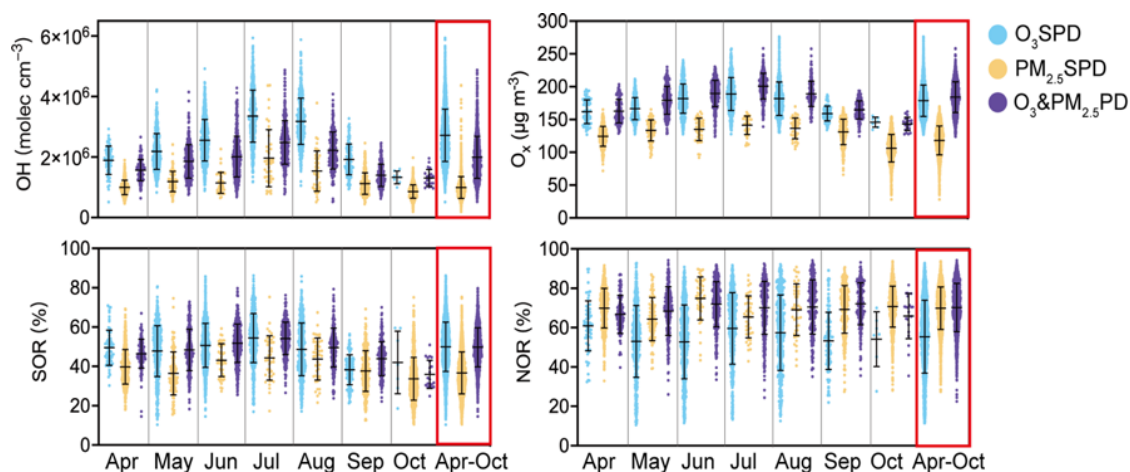
380

381 **Figure 5.** The boxplots of surface-layer hydroxyl radical (OH, molec cm^{-3}), total

382 oxidant (O_x, µg m^{-3}), sulfur oxidation ratio (SOR, %), nitrogen oxidation ratio

383 (NOR, %) for model-captured O_3SPD, $PM_{2.5}$SPD, and O_3&$PM_{2.5}$PD in 18 grids of

384 BTH in the months of April to October from 2013 to 2020. The whiskers represent the

385 standard deviation, the black line represents the mean value of the samples.

386 **3.3.2 Surface-layer concentrations of $PM_{2.5}$ components in O_3SPD, $PM_{2.5}$SPD, and**

387 **O_3&$PM_{2.5}$PD**

388   The simulated concentrations of PM$_{2.5}$ components (NO$_3^-$, NH$_4^+$, SO$_4^{2-}$, BC, and

389   OC, averaged over 18 grids of BTH are shown in Fig. 6 for days of O$_3$SPD, PM$_{2.5}$SPD,

390   and O$_3$&PM$_{2.5}$PD in the warm seasons of 2013-2020 that were observed and also

391   captured by the model. While the mean concentrations of NO$_3^-$, NH$_4^+$, BC, and OC,

392   were all the highest in PM$_{2.5}$SPD, SO$_4^{2-}$ concentration was the highest in O$_3$&PM$_{2.5}$PD.

393   In O$_3$SPD, PM$_{2.5}$SPD, and O$_3$&PM$_{2.5}$PD, the mean concentrations of SO$_4^{2-}$ were 6.2,

394   9.4, and 11.97 µg m^{-3}, respectively, and the percentages of SO$_4^{2-}$ in PM$_{2.5}$ were 14.9%,

395   9.0%, and 15.0%, respectively. In July and August, the concentrations of SO$_4^{2-}$ and

396   MDA8 O$_3$ in O$_3$&PM$_{2.5}$PD were the highest compared with those in O$_3$SPD and

397   PM$_{2.5}$SPD (Fig. S5).
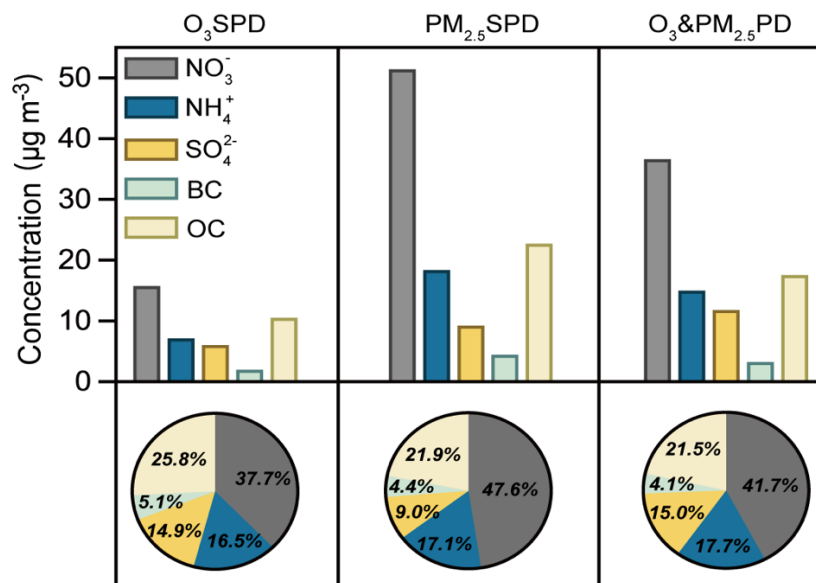
398

399   **Figure 6.** The concentrations of PM$_{2.5}$ components (µg m^{-3}) and percentages of PM$_{2.5}$

400   components (%) at the surface for NO$_3^-$, NH$_4^+$, SO$_4^{2-}$, BC, and OC. The values were

401   averaged over the model-captured O$_3$SPD, PM$_{2.5}$SPD, and O$_3$&PM$_{2.5}$PD in the months

402   of April to October of 2013-2020 in BTH.

403   Figure 7 presents the hourly concentrations of NO$_3^-$, NH$_4^+$, SO$_4^{2-}$, BC, OC, and O$_3$

404   for model-captured O$_3$SPD, PM$_{2.5}$SPD, and O$_3$&PM$_{2.5}$PD over all 18 grids of BTH in

405 the warm seasons from 2013-2020. Concentrations of NO_3^- and NH_4^+ had similarities

406 in diurnal variations, all of which reached the highest values in the early morning (5:00

407 local time (LT) in O_3SPD and O_3&$PM_{2.5}$PD, 7:00-8:00 LT in $PM_{2.5}$SPD) and had the

408 lowest values in the late afternoon (18:00 LT in O_3SPD and O_3&$PM_{2.5}$PD, 16:00 LT in

409 $PM_{2.5}$SPD). Concentrations of BC and OC peaked at the same time as those of NO_3^-

410 and NH_4^+ and had the lowest values at 15:00 LT in O_3SPD, $PM_{2.5}$SPD, and

411 O_3&$PM_{2.5}$PD. The diurnal variations in NO_3^-, NH_4^+, BC, OC reflected the diurnal

412 variations in PBLH (shown in Fig. S6), which generally reached their highest

413 concentrations before the sudden uplift of PBLH in the early morning (times for uplift

414 of PBLH: 6:00 LT in O_3SPD and O_3&$PM_{2.5}$PD, 7:00 LT in $PM_{2.5}$SPD). Compared to

415 O_3SPD and O_3&$PM_{2.5}$PD, the PBLH of $PM_{2.5}$SPD was lower and uplifted one hour

416 later, which was more favorable for the accumulation of aerosols. During the daytime,

417 PBLH in O_3&$PM_{2.5}$PD was between O_3SPD and $PM_{2.5}$SPD.

418   It is worth noting that the diurnal variations of SO_4^{2-} were different from those of

419 other aerosol species, with the highest values at 20:00, 9:00, and 16:00 LT in O_3SPD,

420 $PM_{2.5}$SPD, and O_3&$PM_{2.5}$PD, respectively, and the lowest values in early morning and

421 night (5:00 LT in O_3SPD and O_3&$PM_{2.5}$PD, 23:00 LT in $PM_{2.5}$SPD). For the diurnal

422 variation of O_3, the highest values occurred during the daytime (16:00 LT in O_3SPD

423 and O_3&$PM_{2.5}$PD, 15:00 LT in $PM_{2.5}$SPD) and the lowest values appeared at 5:00 LT

424 in all the cases. Therefore, in O_3&$PM_{2.5}$PD, the time of the highest value of SO_4^{2-} was

425 the same as that of O_3, indicating that SO_4^{2-} and O_3 were produced synergistically

426 during the daytime with strong atmospheric oxidation.
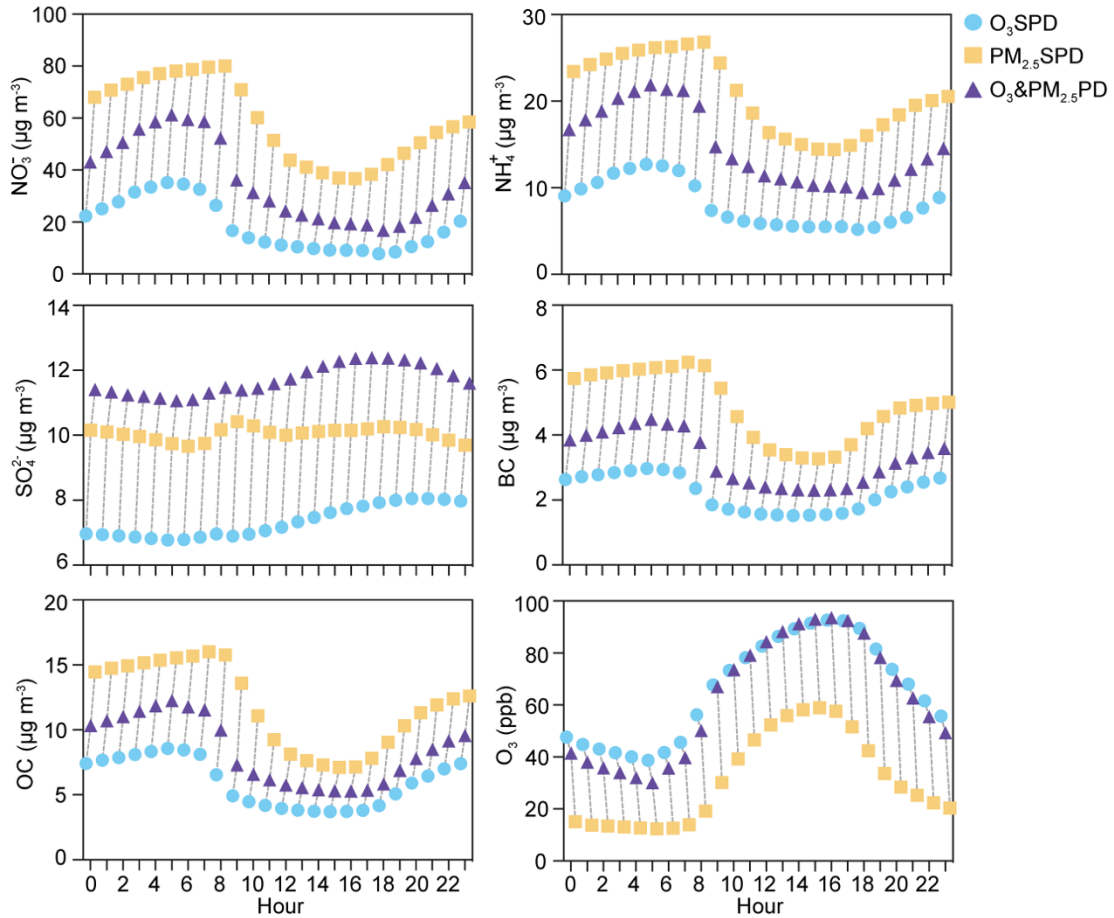
Figure 7. The hourly concentrations of NO_3^-, NH_4^+, SO_4^{2-}, BC, OC, and O_3 averaged over the model-captured O_3SPD, $PM_{2.5}$SPD, and O_3 &$PM_{2.5}$PD in BTH in the months of April to October of 2013-2020.

3.3.3 Vertical distributions of O_3 and $PM_{2.5}$ in O_3SPD, $PM_{2.5}$SPD, and O_3&$PM_{2.5}$PD

The simulated vertical distributions of O_3 and $PM_{2.5}$ averaged over the 18 grids of BTH and the O_3SPD, $PM_{2.5}$SPD, and O_3&$PM_{2.5}$PD in warm seasons of 2013-2020 are shown in Fig. 8. The vertical distribution of O_3 in O_3SPD was similar to that in O_3&$PM_{2.5}$PD (Fig. 8a). In these two cases, concentrations of O_3 increased from the surface to about 975 hPa, remained high between 975 and 819 hPa, and decreased with altitude between 819 and 663 hPa. Although the magnitudes of O_3 were close at the surface (61.9 ppb in O_3&$PM_{2.5}$PD and 58.1 ppb in O_3SPD), the concentration of O_3

440   averaged over 975 and 819 hPa was 10.4% higher in O_3&$PM_{2.5}$PD than in O_3SPD,

441   which was a very unique feature of O_3&$PM_{2.5}$PD. For the case of $PM_{2.5}$SPD, the

442   concentrations of O_3 were the lowest among the three cases and increased gently with

443   altitude above 975 hPa.

444   Figure 8b shows the vertical distributions of $PM_{2.5}$ components. In all the cases,

445     $PM_{2.5}$ concentrations were the highest at the surface, and decreased with altitude from

446   the surface to 975 hPa. However, concentrations of $PM_{2.5}$ were quite stable between

447   975 and 819 hPa for O_3SPD (about 36.4 μg m^{-3}) and O_3&$PM_{2.5}$PD (about 58.1 μg m^{-3}),

448   corresponding to the stable O_3 levels at these altitudes in these two cases (Fig. 8a). For

449     $PM_{2.5}$SPD, while $PM_{2.5}$ concentration at the surface was the highest among the three

450   cases, it decreased rapidly between 975 and 819 hPa. The averaged $PM_{2.5}$ concentration

451   between 975 and 819 hPa was 52.4 μg m^{-3} in $PM_{2.5}$SPD, which was lower than that in

452   O_3&$PM_{2.5}$PD.
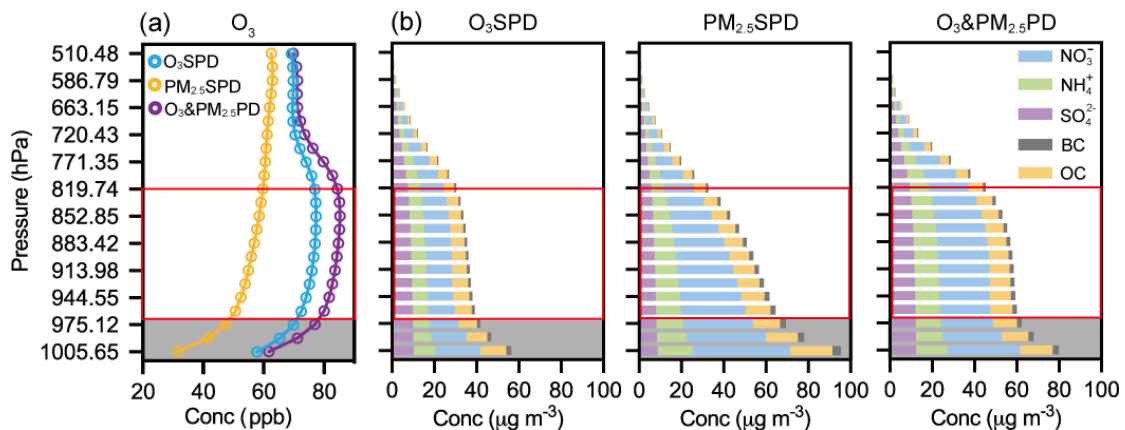
454   **Figure 8.** The vertical distributions of (a) concentrations of O_3 (ppb) and (b) $PM_{2.5}$

455   components (μg m^{-3}) of NO_3^-, NH_4^+, SO_4^{2-}, BC, OC averaged over the model-

456   captured O_3SPD, $PM_{2.5}$SPD, and O_3&$PM_{2.5}$PD in BTH in the months of April to

457   October of 2013-2020.

458   To further investigate the differences in vertical profiles of NO_3^-, NH_4^+, SO_4^{2-}, BC,

OC, and PM$_{2.5}$ in O$_3$SPD, PM$_{2.5}$SPD, and O$_3$&PM$_{2.5}$PD, the ratios of concentration at

975 hPa to that at the surface as well as the concentration at 819 hPa to that at 975 hPa

are shown in Table 1. The concentration of PM$_{2.5}$ decreased largely, with the ratio of

PM$_{2.5(975\ hPa)}$ / PM$_{2.5(1005\ hPa)}$ of 0.78 in O$_3$&PM$_{2.5}$PD and of 0.74 in PM$_{2.5}$SPD. For each

of the PM$_{2.5}$ components, the ratios near the surface (from 1005 to 975 hPa, gray shaded

area in Fig. 8) were close in the three types of pollution. While the ratios of NO$_3^-$, NH$_4^+$,

BC, OC were in the range of 0.65-0.80, the ratios of SO$_4^{2-}$ were about 0.93-0.98,

indicating that SO$_4^{2-}$ concentrations were quite uniform from the surface to 975 hPa in

all three types of pollution.

Table 1. The ratios at 975 and 1005 hPa (gray shaded area in Fig. 8) and at 819 and

975 hPa (red frame in Fig. 8) of NO$_3^-$, NH$_4^+$, SO$_4^{2-}$, BC, OC, and PM$_{2.5}$ in O$_3$SPD,

PM$_{2.5}$SPD, and O$_3$&PM$_{2.5}$PD in BTH region.

		NO$_3^-$	NH$_4^+$	SO$_4^{2-}$	BC	OC	PM$_{2.5}$
Conc$_{819\ hPa}$/ Conc$_{975\ hPa}$	O$_3$SPD	0.95	0.90	0.85	0.73	0.73	0.86
	PM$_{2.5}$SPD	0.64	0.68	0.81	0.64	0.63	0.67
	O$_3$&PM$_{2.5}$PD	0.94	0.91	0.87	0.79	0.77	0.89
Conc$_{975hPa}$/ Conc$_{1005\ hPa}$	O$_3$SPD	0.65	0.77	0.96	0.69	0.70	0.74
	PM$_{2.5}$SPD	0.72	0.76	0.93	0.67	0.65	0.73
	O$_3$&PM$_{2.5}$PD	0.72	0.80	0.98	0.76	0.73	0.78

In the upper layers (975-819 hPa, red rectangle in Fig. 8), the changes in

concentrations of pollutants with altitude in PM$_{2.5}$SPD were quite different from those

in O$_3$&PM$_{2.5}$PD and O$_3$SPD. The decline of PM$_{2.5}$ from 975 to 819 hPa was slow in

O$_3$&PM$_{2.5}$PD (PM$_{2.5(819\ hPa)}$ /PM$_{2.5(975\ hPa)}$ = 0.89) and O$_3$SPD (0.86) and fast in

476 PM$_{2.5}$SPD (0.67). Considering that the variation of BC with altitude was mainly driven

477 by meteorology (Sun et al., 2020), the vertical variations of other components that

478 differed significantly from BC indicated the influences of chemical processes. In

479 PM$_{2.5}$SPD, NO$_3^-$, NH$_4^+$, OC had about the same ratio as BC (0.64) (with large decreases

480 with height), except for SO$_4^{2-}$ concentration that had a ratio of 0.81. In O$_3$&PM$_{2.5}$PD,

481 the ratios of NO$_3^-$, NH$_4^+$, SO$_4^{2-}$ were, 0.94, 0.91, 0.87, respectively, which were much

482 higher than the value of BC (0.79), indicating NO$_3^-$, NH$_4^+$, SO$_4^{2-}$ were quite uniform

483 in the layers of 975-819 hPa with the influence of chemical processes, which will be

484 discussed further in Sect. 3.3.4 below.

485 **3.3.4 Process analyses for O$_3$SPD, PM$_{2.5}$SPD, and O$_3$&PM$_{2.5}$PD**

486   The process analysis (PA) is applied to identify the relative importance of

487 atmospheric processes in the three types of pollution. Figure 9 shows the net changes

488 in O$_3$, NO$_3^-$, NH$_4^+$, SO$_4^{2-}$ by the processes of chemical production (Chem), horizontal

489 advection (Horizontal_adv), vertical advection (Vertical_avd), and diffusion (Diff,

490 vertical PBL mixing process) in the GEOS-Chem model, as well as the total of all these

491 processes (i.e., Chem + Diff + Horizontal_avd + Vertical_avd) in O$_3$SPD, PM$_{2.5}$SPD,

492 and O$_3$&PM$_{2.5}$PD.

493   For O$_3$, the net changes of O$_3$ by all processes were positive at altitudes of 975-

494 819 hPa in O$_3$&PM$_{2.5}$PD and O$_3$SPD, in which Chem had the largest positive

495 contribution (about 1.5 Gg d^{-1}), indicating O$_3$ is chemically produced at these layers.

496 For NO$_3^-$ and NH$_4^+$, the nets of all processes increased mass concentrations at 913-819

497 hPa in O$_3$&PM$_{2.5}$PD and O$_3$SPD, in which Chem and Vertical_avd were positive and

498 Chem had the largest positive contribution. The vertical profiles of Chem were similar

499 for NO$_3^-$ and NH$_4^+$, both of which had the largest positive values at 913-819 hPa (2.83

500 Gg d^{-1} for NO$_3^-$ and 0.88 Gg d^{-1} for NH$_4^+$), leading to higher concentrations of NO$_3^-$

501   and NH_4^+ in O_3&$PM_{2.5}PD$ than in O_3SPD and $PM_{2.5}SPD$. Chem and Diff of SO_4^{2-}

502   were different from those of NO_3^- and NH_4^+. For SO_4^{2-}, Chem was positive from the

503   surface to 510 hPa with a peak around 819 hPa, and Diff was positive at 819-771 hPa

504   but negative from 819 hPa to the surface, which resulted in the uniform SO_4^{2-} profile

505   as shown in Fig. 8. Chem for SO_4^{2-} was the highest around 819 hPa in O_3&$PM_{2.5}PD$,

506   which was related to the strong liquid-phase chemical formation of SO_4^{2-} (Fig. S7). In

507   addition to Chem, Vertical_avd also had positive contributions to the net changes in O_3,

508   NO_3^-, NH_4^+, and SO_4^{2-} at 944-819 hPa. Vertical_avd was negative at 819 hPa and

509   positive between 944 to 819 hPa, implying that the pollutants were transported from

510   819 hPa to 944 hPa in O_3&$PM_{2.5}PD$.
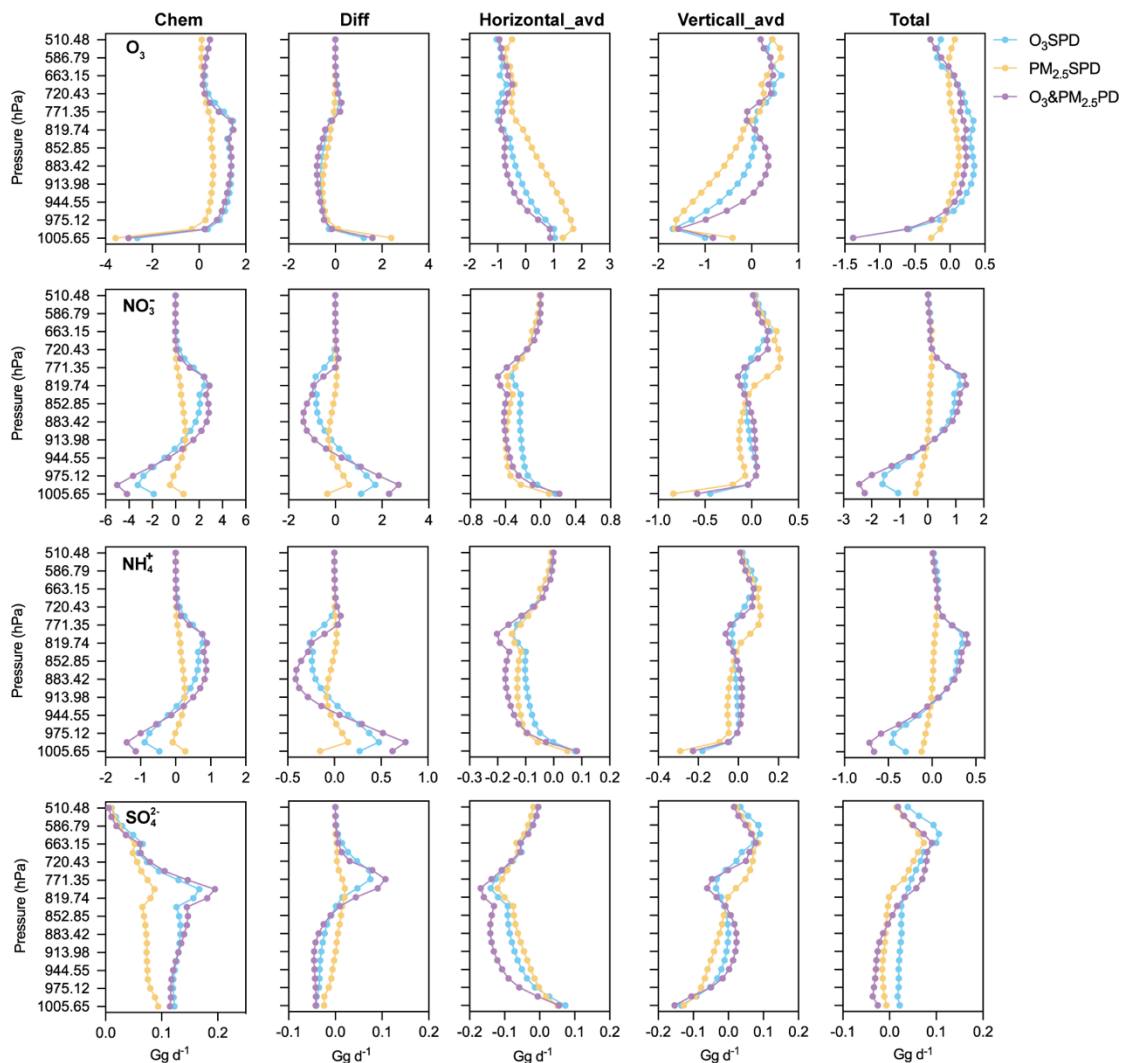
511

512   **Figure 9.** The vertical profiles of net changes in O_3, NO_3^-, NH_4^+, and SO_4^{2-} (Gg d^{-1})

513   over BTH by each and total of processes. The values were averaged over the model-

514   captured regional O_3SPD, PM$_{2.5}$SPD, and O_3&PM$_{2.5}$PD in April-October of 2013-

515   2020.

516   Overall, NO_3^-, NH_4^+, and SO_4^{2-} all had larger chemical productions at 913-819

517   hPa in O_3&PM$_{2.5}$PD compared to those in O_3SPD and PM$_{2.5}$SPD, accompanied by

518   strong vertical transport from 819 hPa to near the surface, resulting in the quite uniform

519   vertical profiles at 975-819 hPa in O_3&PM$_{2.5}$PD. In addition, the vertical profiles of net

520   changes in PM$_{2.5}$ over BTH are shown in Fig. S8 for these three cases. Since NO_3^-,

521   NH_4^+, and SO_4^{2-} were the major components of PM$_{2.5}$, the PA of PM$_{2.5}$ is similar to that

522   of each component.

523   **3.3.5 Observed AOD in O₃SPD, PM₂.₅SPD, and O₃&PM₂.₅PD**

524   To try to support the model result that O_3&PM$_{2.5}$PD had more uniform vertical

525   profile than PM$_{2.5}$SPD from the surface to 819 hPa altitude, we present the scatter plots

526   of observed AOD (at 440 nm and 675 nm) versus observed PM$_{2.5}$ concentrations in

527   O_3SPD, PM$_{2.5}$SPD, and O_3&PM$_{2.5}$PD in Fig. 10. AERONET observations of AOD

528   from 2013 to 2020 are available at three sites in BTH (that is, Beijing (39.97°N, 116.38°

529   E), Beijing-CAMS (39.93°N, 116.31°E), Xianghe (39.75°N, 116.96°E)). At Beijing

530   (39.97°N, 116.38°E), AOD (440nm and 675nm) increased with PM$_{2.5}$ concentration in

531   all three types of pollution. However, under the same levels of surface PM$_{2.5}$

532   concentration, AOD values in O_3&PM$_{2.5}$PD were higher than in PM$_{2.5}$SPD, implying

533   that the column burdens of aerosols were generally higher in O_3&PM$_{2.5}$PD than in

534   PM$_{2.5}$SPD, which may support the unique vertical distribution of PM$_{2.5}$ in O_3&PM$_{2.5}$PD

535   shown in Fig. 8b. The scatter plots at Beijing-CAMS and Xianghe sites are similar and

536   are shown in Fig. S9.

537
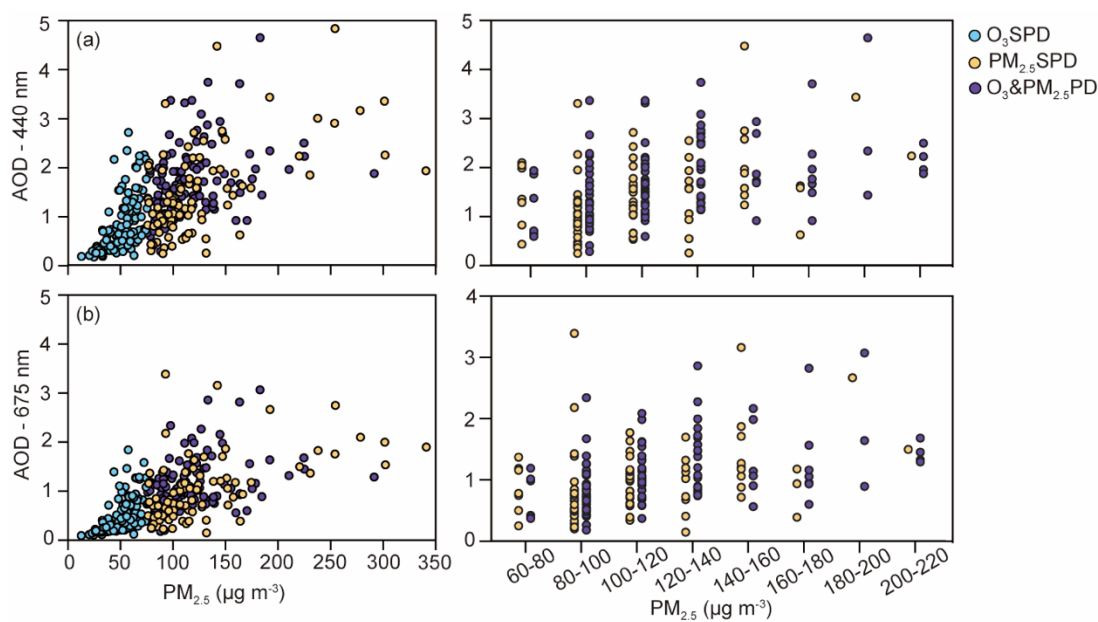
Figure 10. The scatterplots of (a) AOD (440 nm) and (b) AOD (675 nm) versus

observed $PM_{2.5}$ concentrations in O_3SPD, $PM_{2.5}$SPD, and O_3&$PM_{2.5}$PD in Beijing

(39.97°N, 116.38°E) in April-October of 2013-2020.

3.4 Meteorological conditions for O_3SPD, $PM_{2.5}$SPD, and O_3&$PM_{2.5}$PD over BTH

Figure 11 shows the vertical profiles of RH, T, and OMEGA for O_3SPD, $PM_{2.5}$SPD,

and O_3&$PM_{2.5}$PD captured by the model over BTH in the months of April to October

form 2013-2020. It should be noted that O_3&$PM_{2.5}$PD had an unique vertical

distribution of RH. Near the surface, the values of RH in O_3&$PM_{2.5}$PD were between

those in O_3SPD and $PM_{2.5}$SPD. However, in the upper layers (883-771 hPa),

O_3&$PM_{2.5}$PD had the highest RH among the three cases with a peak value of 58.2%.

As a result, the strongest aqueous chemical production of SO_4^{2-} (aqueous oxidation of

SO_2 by H_2O_2) occurred in O_3&$PM_{2.5}$PD around 819 to 771 hPa (Fig. S7**)**. The vertical

profiles of temperature were similar in the three types of pollution, with the lowest

temperature in $PM_{2.5}$SPD. The vertical profiles of OMEGA were different in the three

553 cases. In O$_3$SPD and O$_3$&PM$_{2.5}$PD, OMEGA had positive values around 819 hPa,

554 indicating a strong sinking airflow, leading to a downward transport of pollutants.

555 Under O$_3$&PM$_{2.5}$PD, the average values of PBLH and SWGDN were 946.1 m and

556 257.2 W m^{-2}, respectively, which were higher (lower) than those in PM$_{2.5}$SPD (O$_3$SPD)

557 (Fig. S10).
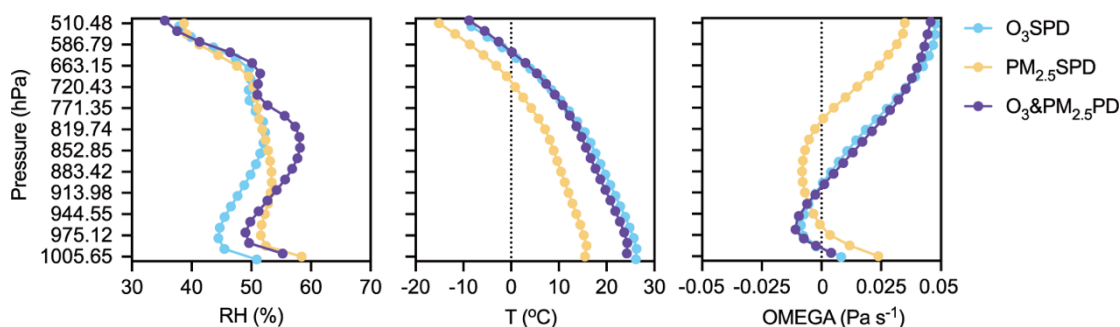
558

559 **Figure 11.** The vertical profiles of RH (%), T (°C), and OMEGA (Pa s^{-1}) averaged over

560 BTH and over the model-captured regional O$_3$SPD, PM$_{2.5}$SPD, and O$_3$&PM$_{2.5}$PD in in

561 April-October of 2013-2020.

562   Figure 12 shows the composited weather patterns for regional O$_3$SPD, PM$_{2.5}$SPD,

563 and O$_3$&PM$_{2.5}$PD (over 50% cities in the BTH experienced the pollution) that were

564 captured by the model in April-October of 2013-2020. The weather patterns of

565 O$_3$&PM$_{2.5}$PD were similar to some extent to those of O$_3$SPD but were quite different

566 from those of PM$_{2.5}$SPD. In O$_3$&PM$_{2.5}$PD, the BTH region was controlled by westerlies

567 and an anomalous high-pressure system at 500 hPa (Figure S11). At 850 hPa, BTH was

568 at the west boundary of an anomalous anticyclone, and the associated strong anomalous

569 southerlies at 850 hPa brought moist air to BTH (Fig. S12 and S13), resulting in a high

570 RH that was beneficial to the aqueous chemical production of SO_4^{2-} in O$_3$&PM$_{2.5}$PD.

571 In O$_3$SPD, BTH was under the influence of the high pressure ridge of the Western

572 Pacific Subtropical High (WPSH) at 850 hPa. Besides, the Northeast Cold Vortex was

573 located to the southwest of BTH at 850 hPa in O$_3$SPD, leading to dry and warm

574 conditions, which was favorable for the formation of O$_3$. In PM$_{2.5}$SPD, the BTH region

575 was under the influence of both the continental high and the WPSH at 850 hPa. At the

576 surface, BTH was under the influence of a uniform high pressure with very weak winds

577 and hence stagnate atmosphere, which was conducive to the accumulation of $PM_{2.5}$.
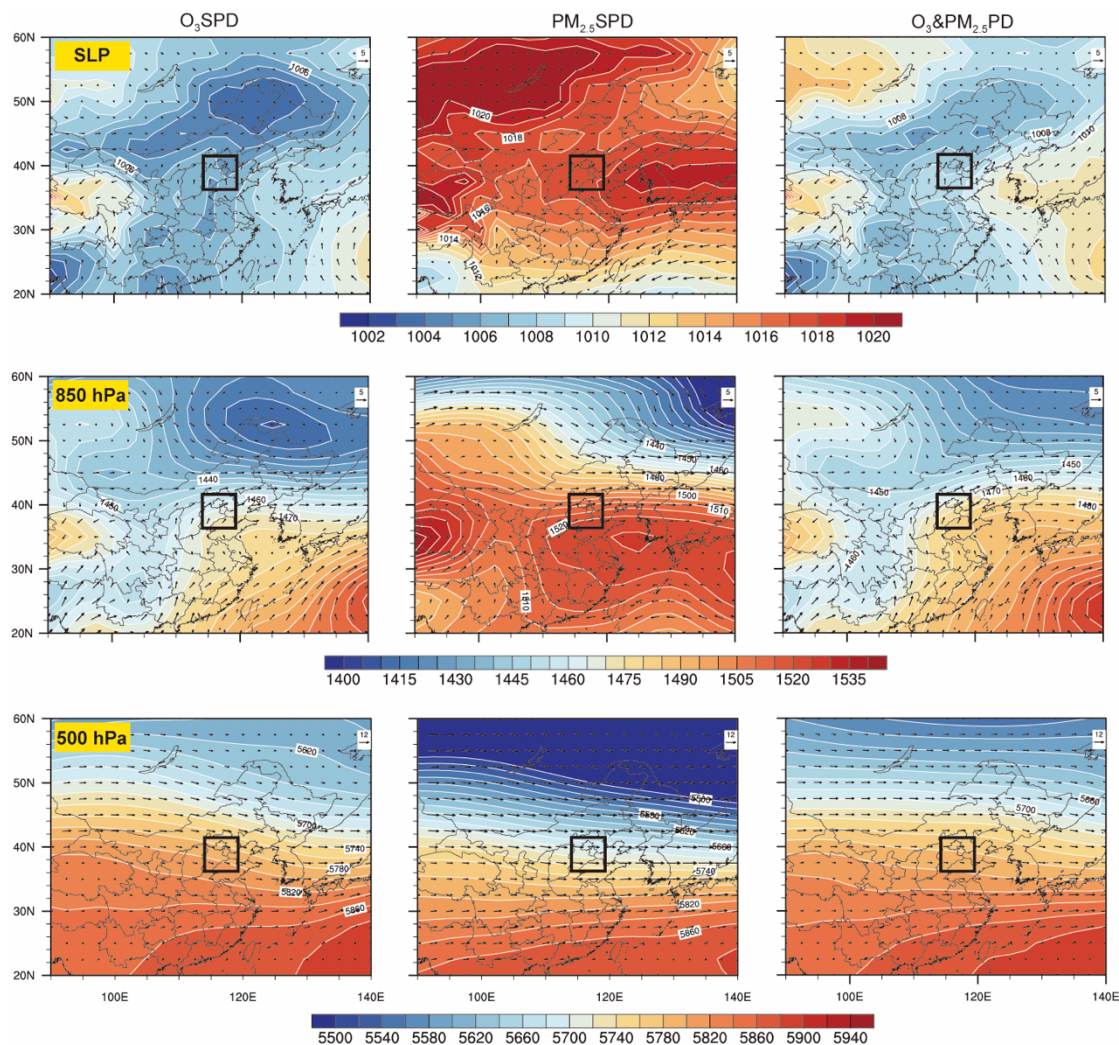
578

579 **Figure 12.** Composites of wind field (m s^{-1}) with SLP (sea level pressure) and with

580 geopotential height at 850 hPa and 500 hPa for regional O_3SPD, $PM_{2.5}$SPD, and

581 O_3&$PM_{2.5}$PD that were captured by the model in April-October of 2013-2020. The

582 solid black rectangle indicates BTH region.

583

584 **4. Conclusions**

585   We used the observed hourly concentrations of O_3 and $PM_{2.5}$ from CNEMC and

586 the model results from the nested-grid version of the GEOS-Chem model to examine

the chemical and physical characteristics of the co-polluted days by O_3 and $PM_{2.5}$

(O_3&$PM_{2.5}$PD) over the BTH region for eight warm seasons (April-October) from

2013 to 2020. The characteristic of O_3&$PM_{2.5}$PD were compared with those of the

polluted days by O_3 alone (O_3SPD) and by $PM_{2.5}$ alone ($PM_{2.5}$SPD). In April-October

of 2013-2020, the observed O_3SPD, $PM_{2.5}$SPD, and O_3&$PM_{2.5}$PD were 2954, 2148,

and 1614 days, respectively, in which 75.0% (2954/3937), 58.1% (2148/3698), and

79.7% (1614/2024) were captured by the GEOS-Chem model, respectively. We

carried out composited analyses of the chemical and physical characteristics for

O_3SPD, $PM_{2.5}$SPD, and O_3&$PM_{2.5}$PD by using the samples (days) captured by both

the observations and the model.

The chemical characteristics of O_3&$PM_{2.5}$PD were found to be different from

those of O_3SPD, $PM_{2.5}$SPD at the surface. O_3&$PM_{2.5}$PD occurred with high levels of

atmospheric oxidants (high OH and O_x), with higher SOR and NOR compared to those

in O_3SPD and $PM_{2.5}$SPD, leading to high concentrations of both O_3 and $PM_{2.5}$. At the

surface, the composited concentrations of NO_3^-, NH_4^+, BC, and OC were the highest in

$PM_{2.5}$SPD, while the composited concentration of SO_4^{2-} was the highest in

O_3&$PM_{2.5}$PD. There was a strong formation of SO_4^{2-} during the daytime in

O_3&$PM_{2.5}$PD in the oxidative atmosphere.

We also found unique features of the vertical distributions of O_3 and $PM_{2.5}$ in

O_3&$PM_{2.5}$PD. Concentrations of $PM_{2.5}$ were stable and high between 975 and 819 hPa

in O_3&$PM_{2.5}$PD, unlike those in $PM_{2.5}$SPD that decreased rapidly with the altitude. In

O_3&$PM_{2.5}$PD, the vertical profiles of NO_3^-, NH_4^+, and SO_4^{2-} were quite uniform at

975-819 hPa, corresponding to the stable O_3 concentrations at these altitudes. The

process analysis (PA) showed that NO_3^-, NH_4^+, and SO_4^{2-} all had larger chemical

productions at altitudes of 913-819 hPa in O_3&$PM_{2.5}$PD compared to those in O_3SPD

and PM$_{2.5}$SPD. The chemical production of SO_4^{2-} had large positive values from the surface to about 500 hPa. The Vertical_avd also had positive contributions to the net changes in O$_3$, NO_3^-, NH_4^+, and SO_4^{2-} at 944-819 hPa in O$_3$&PM$_{2.5}$PD. Therefore, the strong chemical productions at 913-819 hPa accompanied by the downward transport resulted in the quite uniform vertical profiles at 975-819 hPa in O$_3$&PM$_{2.5}$PD.

Figure 13 summarizes the chemical and physical characteristics in O$_3$&PM$_{2.5}$PD, O$_3$SPD, and PM$_{2.5}$SPD in the BTH region. In O$_3$&PM$_{2.5}$PD, the strong chemical productions of O$_3$, NO_3^-, NH_4^+, and SO_4^{2-} occurred at high altitudes of 913-819 hPa where RH was high, and the accompanied downward airflow caused the stable concentrations at 944-819 hPa. The composited PBLH in O$_3$&PM$_{2.5}$PD was about 946.1 m, and the strong mixed diffusion underneath the PBLH led to high concentrations of pollutants at the ground level. In contrast, O$_3$SPD occurred in hot and dry atmosphere with composited PBLH of 1073.5 m. Strong O$_3$ chemical production occurred around 819 hPa, and O$_3$ was then transported to the surface by downward air flow. The atmosphere was stable and stagnate when PM$_{2.5}$SPD occurred, with the lowest PBLH of 681.8 m. High RH (high chemical formation of PM$_{2.5}$) and the accumulation of aerosols led to the highest surface-layer PM$_{2.5}$ in PM$_{2.5}$SPD.

To summarize, O$_3$&PM$_{2.5}$PD were characterized by high O$_x$, SOR, and NOR, uniform vertical profiles at 975-819 hPa, which were caused by an anomalous high-pressure system at 500 hPa, strong southerlies and high RH at 850 hPa. Meteorological parameters around 850 hPa promoted strong chemical production of secondary aerosols and downward transport, resulting in the unique vertical profiles and high surface concentrations in O$_3$&PM$_{2.5}$PD.

635
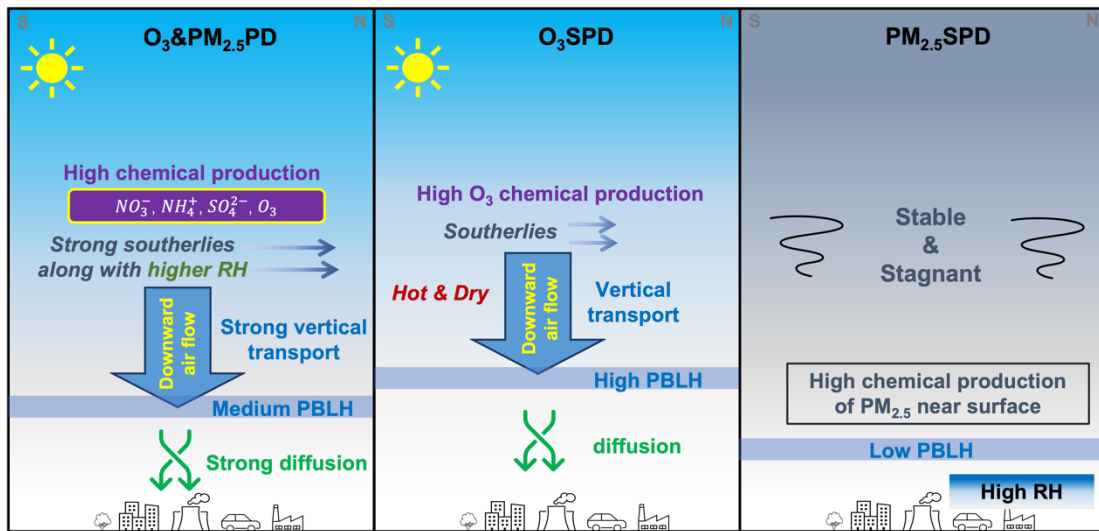
Figure 13. A schematic diagram of chemical and physical and characteristics in

O₃SPD, PM₂.₅SPD, and O₃&PM₂.₅PD in BTH region.

Data availability.

The GEOS-Chem model is available at https://geos-chem.seas.harvard.edu (last access: 17 November 2022). The observed hourly surface concentrations of air pollutants are derived from the China National Environ- mental Monitoring Center (https://air.cnemc.cn:18007/, last access: 17 November 2022). The simulation results are available upon request from the corresponding author (hongliao@nuist.edu.cn).

Author contributions.

HD and HL conceived the study and designed the experiments. HD performed model simulations and analysed the data. KL, XY, YY, JZ, JJ, and BL provided useful comments on the paper. HD and HL prepared the paper, with contributions from all co-authors.

Competing interests.

The authors declare that they have no conflict of interest.

Acknowledgements.

We acknowledge the CNEMC for making their data publicly available. We acknowledge the efforts of GEOS-Chem working groups for developing and managing the model.

Financial support.

660   This work was supported by the National Natural Science Foundation of China (Grant

661   No. 42021004), the National Key Research and Development Program of China

662   (Grant No. 2019YFA0606800), and the Carbon Peak Carbon Neutral Science and

663   Technology Innovation Foundation of Jiangsu Province (BK20220031).

664

References

Alexander, B., Park, R. J., Jacob, D. J., Li, Q. B., Yan- tosca, R. M., Savarino, J., Lee, C. C. W., and Thiemens, M. H.: Sulfate formation in sea-salt aerosols: Constraints from oxygen isotopes, J. Geophys. Res.-Atmos., 110, D10307, https://doi.org/10.1029/2004jd005659, 2005.

Bey, I., Jacob, D. J., Yantosca, R. M., Logan, J. A., Field, B. D., Fiore, A. M., Li, Q. B., Liu, H. G. Y., Mickley, L. J., and Schultz, M. G.: Global modeling of tropospheric chemistry with assimilated meteorology: Model description and evaluation, J. Geophys. Res.-Atmos., 106, 23073–23095, https://doi.org/10.1029/2001jd000807, 2001.

Chu, B. W., Ma, Q. X., Liu, J., Ma, J. Z., Zhang, P., Chen, T. A., Feng, Q. C., Wang. C. Y., Yang, N., Ma, H. N., Ma, J. J., Russell, A. G., He, H.: Air Pollutant Correlations in China: Secondary Air Pollutant Responses to NO_x and SO_2 Control, Environ. Sci. Tech. Let., 7(10), 695-700, http://dx.doi.org/10.1021/acs.estlett.0c00403, 2020.

Dai, H. B., Zhu, J., Liao, H., Li, J. D., Liang, M. X., Yang, Y., Yue, X.: Co-occurrence of ozone and $PM_{2.5}$ pollution in the Yangtze River Delta over 2013-2019: spatiotemporal distribution and meteorological conditions, Atmos. Res., 249, 105363, https://doi.org/10.1016/j.atmosres.2020.105363, 2021.

Dang, R. J. and Liao, H.: Severe winter haze days in the Beijing-Tianjin-Hebei region from 1985-2017 and the roles of anthropogenic emissions and meteorology, Atmos. Chem. Phys., 19, 10801-10816, https://doi.org/10.5194/acp-19-10801-2019, 2019.

Dang, R. J., Liao, H., and Fu, Y.: Quantifying the anthropogenic and meteorological influences on summertime surface ozone in China over 2012-2017, Sci. Total. Environ., 754, 142394, https://doi:10.1016/j.scitotenv.2020.142394, 2021.

Duan, F., He, K., Ma, Y., Yang, F., Yu, X., Cadle, S. H., Chan, T., and Mulawa, P. A.: Concentration and chemical characteristics of PM2.5 in Beijing, China: 2001–2002, Sci. Total Environ., 355(1–3), 264–275, https://doi:10.1016/j.scitotenv.2005.03.001, 2006.

Fairlie, T. D., Jacob, D. J., and Park, R. J.: The impact of transpacific transport of mineral dust in the United States, Atmos. Environ., 41, 1251–1266, https://doi.org/10.1016/j.atmosenv.2006.09.048, 2007.

Gao, Y. and Ji, H. B.: Microscopic morphology and seasonal variation of health effect arising from heavy metals in $PM_{2.5}$ and PM_{10}: One-year measurement in a densely populated area of urban Beijing, Atmos. Res., 212, 213–226, https://doi.org/10.1016/j.atmosres.2018.04.027, 2018.

Giles, D. M., Sinyuk, A., Sorokin, M. S., Schafer, J. S., Lyapustin, A.: Advancements in the aerosol robotic network (aeronet) version 3 database – automated near real-time quality control algorithm with improved cloud screening for sun photometer aerosol optical depth (aod) measurements, Atmos. Meas. Tech., 12, 169–209, https://doi.org/10.5194/amt-12-169-2019. 2019.

Gonçalves, M., Jiménez-Guerrero, P., and Baldasano, J. M.: Contribution of atmospheric processes affecting the dynamics of air pollution in South-Western Europe during a typical summer-time photochemical episode, Atmos. Chem. Phys.,

709   9, 849–864, https://doi.org/10.5194/acp-9-849-2009, 2009.

710   Gong, C. and Liao, H.: A typical weather pattern for the ozone pollution events in North

711   China, Atmos. Chem. Phys., 19, 13725-13740, https://doi.org/10.5194/acp-19-

712   13725-2019, 2019.

713   Gong, C., Liao, H., Zhang, L., Yue, X., Dang, R. J., Yang, Y.: Persistent ozone pollution

714   episodes in North China exacerbated by regional transport, Environ. Pollut., 265,

715   115056, https://doi:10.1016/j.envpol.2020.115056, 2020.

716   Guenther, A. B., Jiang, X., Heald, C. L., Sakulyanontvittaya, T., Duhl, T., Emmons, L.

717   K., and Wang, X.: The Model of Emissions of Gases and Aerosols from Nature

718   version 2.1 (MEGAN2.1): an extended and updated framework for mod- eling

719   biogenic emissions, Geosci. Model Dev., 5, 1471–1492,

720   https://doi.org/10.5194/gmd-5-1471-2012, 2012.

721   Jiang, N., Li, L., Wang, S., Li, Q., Dong, Z., Duan, S., Zhang, R., Li, S.: Variation

722   tendency of pollution characterization, sources, and health risks of $PM_{2.5}$-bound

723   polycyclic aromatic hydrocarbons in an emerging megacity in China: based on

724   three-year data, Atmos. Res., 217, 81–92, https://doi.org/10.1016/j.

725   atmosres.2018.10.023, 2019.

726   Li, K., Jacob, D. J., Liao, H., Zhu, J., Shah, V., Shen, L., Bates, K., Zhang, Q., Zhai, S.

727   X.: A two-pollutant strategy for improving ozone and particulate air quality in

728   China, Nat. Geosci., 12, 906–910, https://doi.org/10.1038/s41561-019-0464-x,

729   2019.

730   Li, K., Jacob, D. J., Shen, L., Lu, X., Smedt, D. I., Liao, H.: Increases in surface ozone

pollution in China from 2013 to 2019: anthropogenic and meteorological influences, Atmos. Chem. Phys., 20, 11423-11433, https://doi.org/10.5194/acp-20-11423-2020, 2020.

Li, M., Wang, L., Liu, J.: Exploring the regional pollution characteristics and meteorological formation mechanism of $PM_{2.5}$ in North China during 2013-2017, Environ. Int., 134, 105283, https://doi.org/10.1016/j.envint.2019.105283, 2019.

Li, M., Zhang, Q., Kurokawa, J.-I., Woo, J.-H., He, K., Lu, Z., Ohara, T., Song, Y., Streets, D. G., Carmichael, G. R., Cheng, Y., Hong, C., Huo, H., Jiang, X., Kang, S., Liu, F., Su, H., and Zheng, B.: MIX: a mosaic Asian anthropogenic emission inventory under the international collaboration framework of the MICS-Asia and HTAP, Atmos. Chem. Phys., 17, 935–963, https://doi.org/10.5194/acp-17-935-2017, 2017.

Liu, Y. X., Zhao, Q. B., Hao, X., Zhao, J. R., Zhang, Y., Yang, X., Fu, Q. Y., Xu, X. Y., Wang, X. F., Huo, J. T., Chen, J. M.: Increasing surface ozone and enhanced secondary organic carbon formation at a city junction site: An epitome of the Yangtze River Delta, China (2014–2017), Environ. Pollut., 265, 0269-7491, https://doi.org/10.1016/j.envpol.2020.114847, 2020.

Lou, S. J., Liao, H., Yang, Y., and Mu, Q.: Simulation of the interannual variations of tropospheric ozone over China: Roles of variations in meteorological parameters and anthropogenic emissions, Atmos. Environ., 122, 839–851, https://doi.org/10.1016/j.atmosenv.2015.08.081, 2015.

Molod, A., Takacs, L., Suarez, M., and Bacmeister, J.: Development of the GEOS-5

atmospheric general circulation model: evolution from MERRA to MERRA2, Geosci. Model Dev., 8, 1339–1356, https://doi.org/10.5194/gmd-8-1339-2015, 2015.

Mu, Q. and Liao, H.: Simulation of the interannual varia- tions of aerosols in China: role of variations in meteo- rological parameters, Atmos. Chem. Phys., 14, 9597– 9612, https://doi.org/10.5194/acp-14-9597-2014, 2014.

Nan, J. L., Wang, S. S., Guo, Y. L., Xiang, Y. J., Zhou. B.: Study on the daytime OH radical and implication for its relationship with fine particles over megacity of Shanghai, China, Atmos. Environ., 154, 167-178, https://doi.org/10.1016/j.atmosenv.2017.01.046, 2017.

Ni, R., Lin, J., Yan, Y., and Lin, W.: Foreign and domestic contributions to springtime ozone over China, Atmos. Chem. Phys., 18, 11447–11469, https://doi.org/10.5194/acp-18-11447- 2018, 2018.

Park, R. J., Jacob, D. J., Chin, M., and Martin, R. V.: Sources of carbonaceous aerosols over the United States and implica- tions for natural visibility, J. Geophys. Res.-Atmos., 108, 4355, https://doi.org/10.1029/2002jd003190, 2003.

Park, R. J., Jacob, D. J., Field, B. D., Yantosca, R. M., and Chin, M.: Natural and transboundary pollution influences on sulfate-nitrate-ammonium aerosols in the United States: Im- plications for policy, J. Geophys. Res.-Atmos., 109, D15204, https://doi.org/10.1029/2003jd004473, 2004.

Pye, H. O. T., Liao, H., Wu, S., Mickley, L. J., Jacob, D. J., Henze, D. K., and Seinfeld, J. H.: Effect of changes in climate and emissions on future sulfate-nitrate-

ammonium aerosol lev- els in the United States, J. Geophys. Res.-Atmos., 114, D01205, https://doi.org/10.1029/2008jd010701, 2009.

Qin, Y., Li, J. Y., Gong, K. J., Wu, Z., Chen, M. D., Qin, M. M., Huang, L., Hu, J. L.: Double high pollution events in the Yangtze River Delta from 2015 to 2019: Characteristics, trends, and meteorological situations, Sci. Total. Environ., 792, 148349, https://doi.org/10.1016/j.scitotenv.2021.148349, 2021.

Ren, W., Tian, H., Tao, B., Chappelka, A., Sun, G., Lu, C., Liu, M., Chen, G., Xu, X.: Impacts of tropospheric ozone and climate change on net primary productivity and net carbon exchange of China's forest ecosystems, Glob. Ecol. Biogeogr., 20, 391–406, https://doi.org/10.1111/j.1466-8238.2010.00606.x, 2011.

Sun, T., Wu, C. and Wu, D.: Time-resolved black carbon aerosol vertical distribution measurements using a 356-m meteorological tower in Shenzhen, Theor. Appl. Climatol., 140, 1263–1276, https://doi.org/10.1007/s00704-020-03168-6, 2020.

Tan, Z. F., Fuchs, H., and Lu, K. D.: Radical chemistry at a rural site (Wangdu) in the North China Plain: Observation and model calculations of OH, HO_2 and RO_2 radicals, Atmos. Chem. Phys., 17(1): 663−690, https://doi.org/10.5194/acp-17-663-2017, 2017.

Wang, H., Kiang, C., Tang, X., Zhou, X., Chameides, W. L.: Surface ozone: a likely threat to crops in Yangtze delta of China, Atmos. Eviron., 39, 3843–3850, https://doi. org/10.1016/j.atmosenv.2005.02.057, 2005.

Wang, X., Manning, W., Feng, Z., Zhu, Y.: Ground-level ozone in China: distribution and effects on crop yields, Environ. Pollut., 147 (2), 394–400, https://

797   doi.org/10.1016/j.envpol.2006.05.006, 2007.

798   Woodward-Massey, R., Slater, E. J., Alen, J.: Implementation of a chemical background

799   method for atmospheric OH measurements by laser-induced fluorescence:

800   characterisation and observations from the UK and China, Atmos. Meas. Tech.,

801   13(6): 3119−3146, https://doi.org/10.5194/amt-13-3119-2020, 2020.

802   Xuan, J., Liu, G., and Du, K.: Dust emission inventory in northern China, Atmos.

803   Environ., 34(26), 4565–4570, https://doi:10.1016/S1352-2310(00) 00203-X, 2000.

804   Ye, B., Ji, X., Yang, H., Yao, X., Chan, C. K., Cadle, S. H., Chan, T., and Mulawa, P.

805   A.: Concentration and chemical composition of PM2.5 in Shanghai for a 1-year

806   period, Atmos. Environ., 37(4), 499–510, https://doi:10.1016/S1352-

807   2310(02)00918-4, 2003.

808   Yue, X., Unger, N., Harper, K., Xia, X., Liao, H., Zhu, T., Xiao, J., Feng, Z., Li, J.:

809   Ozone and haze pollution weakens net primary productivity in China, Atmos.

810   Chem. Phys., 17, 6073–6089, https://doi.org/10.5194/acp-2016-1025, 2017.

811   Zhang, Y. and Wang, Y.: Climate-driven ground-level ozone extreme in the fall over the

812   Southeast United States, P. Natl. Acad. Sci. USA, 113, 10025–10030,

813   https://doi.org/10.1073/pnas.1602563113, 2016.

814   Zhao, X. J., Zhao, P. S., Xu, J., Meng, W., Pu, W. W., Dong, F., He, D., and Shi, Q. F.:

815   Analysis of a winter regional haze event and its formation mechanism in the North

816   China Plain, Atmos. Chem. Phys., 13, 5685–5696, https://doi:10.5194/acp-13-

817   5685-2013, 2013.

818   Zheng, B., Tong, D., Li, M., Liu, F., Hong, C., Geng, G., Li, H., Li, X., Peng, L., Qi, J.,

Yan, L., Zhang, Y., Zhao, H., Zheng, Y., He, K., and Zhang, Q.: Trends in China's anthropogenic emissions since 2010 as the consequence of clean air actions, Atmos. Chem. Phys., 18, 14095–14111, https://doi.org/10.5194/acp-18-14095-2018, 2018.

Zheng, B., Zhang, Q., Geng, G., Chen, C., Shi, Q., Cui, M., Lei, Y., He, K.: Changes in China's anthropogenic emissions and air quality during the COVID-19 pandemic in 2020, Earth Syst. Sci. Data, 13, 2895–2907, https://doi.org/10.5194/essd-13-2895-2021, 2021.

Zhu, J., Chen, L., Liao, H., Dang, R. J.: Correlations between $PM_{2.5}$ and ozone over China and associated underlying reasons, Atmosphere, 10(7), 352, https://doi.org/10.3390/atmos10070352, 2019.

Zong, L., Yang, Y., and Gao, M.: Large-scale synoptic drivers of co-occurring summertime ozone and $PM_{2.5}$ pollution in eastern China, Atmos. Chem. Phys., 11, 9105-9124, https://doi.org/10.5194/acp-21-9105-2021, 2021.